Immersed boundary - lattice Boltzmann mesoscale method for wetting problems

Elisa Bellantoni,[1,2,3,*] Fabio Guglietta,[2] Francesca Pelusi,[4] Mathieu Desbrun,[5]
Kiwon Um,[3] Mihalis Nicolaou,[1] Nikos Savva,[1,6] and Mauro Sbragaglia[2]

[1] *Computation-based Science and Technology Research Center, The Cyprus Institute, 20 Konstantinou Kavafi Street, 2121 Nicosia, Cyprus*
[2] *Department of Physics & INFN, Tor Vergata University of Rome, Via della Ricerca Scientifica 1, 00133 Rome, Italy*
[3] *LTCI, Télécom Paris, IP Paris, 19 Place Marguerite Perey, 91120 Palaiseau, France*
[4] *Istituto per le Applicazioni del Calcolo, CNR - Via Pietro Castellino 111, 80131 Naples, Italy*
[5] *Inria Saclay and LIX, IP Paris, 1 rue Honoré d'Estienne d'Orves, 91120 Palaiseau, France*
[6] *Department of Mathematics and Statistics, University of Cyprus, 1 Panepistimiou Avenue, 2109 Nicosia, Cyprus*

We develop a mesoscale computational model to describe the interaction of a droplet with a solid. The model is based on the hybrid combination of the immersed boundary and the lattice Boltzmann computational schemes: the former is used to model the non-ideal sharp interface of the droplet coupled with the inner and outer fluids, simulated with the lattice Boltzmann scheme. We further introduce an interaction force to model the wetting interactions of the droplet with the solid at mesoscale: this interaction force is designed with the key computational advantage of providing a regularization of the interface profile close to the contact line, avoiding abrupt curvature changes that could otherwise cause numerical instabilities. The proposed model substantially improves earlier immersed boundary - lattice Boltzmann models for wetting in that it allows a description of an ample variety of wetting interactions, ranging from hydrophobic to hydrophilic cases, without the need for any pre-calibration study on model parameters to be used. Model validations against analytical results for droplet shape at equilibrium and scaling laws for droplet spreading dynamics are addressed.

I. INTRODUCTION

Understanding the interaction between a liquid droplet and a solid substrate is a complex multiscale problem living at the crossroads between physics, chemistry, and engineering. At macroscopic scales, the ability of a droplet to wet a solid substrate is primarily quantified by the equilibrium contact angle $\theta_{\rm eq}$ via the celebrated Young's law [1, 2],

$$\cos\theta_{\rm eq} = \frac{\sigma_{\rm sg} - \sigma_{\rm sl}}{\sigma} \ ,$$

where σ is the surface tension between the liquid (l) and the ambient gas (g), while $\sigma_{\rm sl}$ and $\sigma_{\rm sg}$ represent the surface tensions between the solid (s) and the liquid and gas, respectively. When a droplet is deposited on a solid substrate, a spreading process follows until an equilibrium shape with contact angle $\theta_{\rm eq}$ is achieved. This spreading process has been the subject of intense scrutiny over the years, including experiments, theory, and numerical simulations [1–5]. In this landscape, numerical simulations are optimal analysis tools, capable of revealing complex features of wetting dynamics [4–29]. Many recent studies [5, 30–36] feature problems with complex interfaces, with added physical richness in comparison to models that account for surface tension forces alone; hence, the development of novel/improved numerical methods displaying flexibility and computational efficiency in modeling complex interface physics for wetting is highly desirable.

The hybrid immersed boundary (IB) - lattice Boltzmann (LB) method is well suited to capture complex interface dynamics [37, 38]. In this approach, the interface is sharp and is usually represented by a mesh on which the desired interface properties are introduced. In addition, the method is based on the LB approach, which is a highly efficient technique in computational fluid dynamics [37–39]. Recent studies have used the IB-LB approach to model soft particles with complex interfaces featuring viscoelasticity [28, 40–49]; however, to the best of our knowledge, applications of IB-LB to wetting problems have been much less studied in the literature. In Ref. [28], Pelusi and co-workers proposed a computational model based on the IB-LB method to simulate the wetting dynamics of coated droplets. In their work, the interaction between the droplet and the solid substrate has been modelled via a Lennard-Jones interaction, which depends on two parameters that must be pre-calibrated to obtain the correct equilibrium contact angle. Moreover, as the authors stated, their implementation can capture only large contact angles. These issues are addressed in the present study via a systematic analytical control of the static solutions, thus avoiding pre-calibration efforts and substantially improving the model applicability in various physical scenarios.

To facilitate comparison with literature results, we focus on the case of a droplet with surface tension σ at the interface. On the one hand, we aim to design and implement an interaction force with the wall that allows controlled modeling of the equilibrium contact angle

* e.bellantoni@cyi.ac.cy

$\theta_{\rm eq}$, i.e., without the need for any pre-calibration step; on the other hand, we aim to extend the applicability of the model to address a broad spectrum of contact angles, ranging from hydrophobic to hydrophilic cases. To validate our IB-LB method, we perform comprehensive comparisons against analytical results for droplet shapes at equilibrium and for droplet dynamics during spreading.

The paper is organized as follows: in Sec. II, we review the basic features of the IB-LB method and describe the way wetting interactions with a solid substrate are introduced in the model; in Sec. III, we report on the results of numerical simulations for both droplet statics and dynamics, with comparisons against known analytical results; conclusions follow in Sec. IV.

II. NUMERICAL METHOD

In this section, we provide details on the numerical method employed. The lattice Boltzmann (LB) method is used to resolve the fluids inside and outside the droplet, while the immersed boundary (IB) method is used to couple the droplet interface with the fluid. A wall-interaction force is further supplied to the IB scheme to model wettability. In Sec. II A, we recall the essential features of the IB-LB method; in Sec. II B, we detail the modeling of surface tension forces; finally, in Sec. II C we give specifics on the modeling of wettability.

A. Immersed-boundary lattice Boltzmann (IB-LB) method

The IB-LB is a well-established method in the literature which is particularly suitable to reproduce flows and their coupling with deformable and complex interfaces [38, 40–51]. Fluid flows are described in terms of continuous fields depending on space position ($\boldsymbol{x}$) and time (t) via the continuity and Navier-Stokes equations:

$$\frac{\partial \rho}{\partial t} + \boldsymbol{\nabla}\cdot(\rho \boldsymbol{U}) = 0 \ , \tag{1}$$

$$\rho\left[\frac{\partial \boldsymbol{U}}{\partial t} + (\boldsymbol{U}\cdot\boldsymbol{\nabla})\boldsymbol{U}\right] = -\boldsymbol{\nabla} p + \mu\nabla^2\boldsymbol{U} + \boldsymbol{F} \ , \tag{2}$$

with $\rho = \rho(\boldsymbol{x},t)$ being the fluid density, $\boldsymbol{U} = \boldsymbol{U}(\boldsymbol{x},t)$ the fluid velocity, $p = p(\boldsymbol{x},t)$ the fluid pressure, μ the dynamic viscosity, and $\boldsymbol{F} = \boldsymbol{F}(\boldsymbol{x},t)$ the force density. The LB method recovers this description by following a kinetic approach, which evolves in time a *discrete* probability distribution function (PDF), $f_i(\boldsymbol{x},t)$, corresponding to the probability density function of finding a fluid particle in the position $\boldsymbol{x}$ at time t having velocity $\boldsymbol{c}_i$. Space positions are discretized on a regular Cartesian lattice with a constant lattice spacing Δx in all directions; correspondingly, time is discretized with a constant time step amplitude Δt. In LB models, a finite set of Q velocity vectors ($i = 0, \ldots, Q-1$) is considered, along which the PDFs can stream [37, 38, 52]. Specifically, this work employs a D3Q19 velocity LB scheme featuring 19 velocity directions ($\boldsymbol{c}_i$) in a three-dimensional lattice. Velocity vectors are associated with statistical weights ω_i. Details about the scheme are reported in Tab. I. The LB equations give the dynamic evolution of all the f_i, providing a version of the Boltzmann equation discretized in time, coordinate, and velocity space [37, 38, 52]:

i	$\boldsymbol{c}_i$	ω_i
0	$(0,0,0)$	1/3
$1-6$	$(\pm\frac{\Delta x}{\Delta t},0,0)$, $(0,\pm\frac{\Delta x}{\Delta t},0)$, $(0,0,\pm\frac{\Delta x}{\Delta t})$	1/18
$7-18$	$(\pm\frac{\Delta x}{\Delta t},\pm\frac{\Delta x}{\Delta t},0)$, $(0,\pm\frac{\Delta x}{\Delta t},\pm\frac{\Delta x}{\Delta t})$, $(\pm\frac{\Delta x}{\Delta t},0,\pm\frac{\Delta x}{\Delta t})$	1/36

TABLE I. Velocity vectors $\boldsymbol{c}_i$ and weights ω_i for the D3Q19 LB scheme.

$$f_i(\boldsymbol{x}+\boldsymbol{c}_i\Delta t, t+\Delta t) - f_i(\boldsymbol{x},t) = \Delta t\left[\Omega_i(\boldsymbol{x},t) + S_i(\boldsymbol{x},t)\right] \ . \tag{3}$$

Eq. (3) represents the sum of a streaming step (left-hand side), in which the populations are advected from one lattice node to another along the velocity vectors $\boldsymbol{c}_i$, and a collision process embedded in the collision term $\Omega_i(\boldsymbol{x},t)$. Streaming and collision steps are further supplemented by external body forces through a source term $S_i(\boldsymbol{x},t)$. In this work, we employ the widely popular Bhatnagar-Gross-Krook (BGK) collision operator which is given by [53]

$$\Omega_i(\boldsymbol{x},t) = -\frac{1}{\tau_{\rm LB}}\left[f_i(\boldsymbol{x},t) - f_i^{(\rm eq)}(\boldsymbol{x},t)\right] \ , \tag{4}$$

where $\tau_{\rm LB}$ is a characteristic relaxation time and $f_i^{(\rm eq)}(\boldsymbol{x},t)$ is the Maxwell-Boltzmann equilibrium distribution function that depends on $(\boldsymbol{x},t)$ via the density and velocity fields, i.e., $f_i^{(\rm eq)}(\boldsymbol{x},t) = f_i^{(\rm eq)}(\rho(\boldsymbol{x},t),\boldsymbol{U}(\boldsymbol{x},t))$. The equilibrium distribution is taken as the Taylor expansion of the Maxwell-Boltzmann distribution up to second order, i.e.,

$$f_i^{(\rm eq)}(\rho,\boldsymbol{U}) = \omega_i\rho\left[1 + \frac{\boldsymbol{U}\cdot\boldsymbol{c}_i}{c_{\rm s}^2} + \frac{(\boldsymbol{U}\cdot\boldsymbol{c}_i)^2}{2c_{\rm s}^4} - \frac{\boldsymbol{U}\cdot\boldsymbol{U}}{2c_{\rm s}^2}\right] . \tag{5}$$

Here, $c_{\rm s}$ is the lattice speed of sound, which corresponds to $c_{\rm s} = \Delta x/(\sqrt{3}\Delta t)$ in the case of the D3Q19 velocity scheme. Higher-order collision operators are possible, but they elude the scope of the present work. The contribution of the force density $\boldsymbol{F}(\boldsymbol{x},t)$ is encoded in the source term $S_i(\boldsymbol{x},t)$, which, in turn, depends on $(\boldsymbol{x},t)$ via the velocity and the force density, i.e., $S(\boldsymbol{x},t) = S(\boldsymbol{U}(\boldsymbol{x},t),\boldsymbol{F}(\boldsymbol{x},t))$, according to the Guo's forcing scheme [54]

$$S_i(\boldsymbol{U},\boldsymbol{F}) = \left(1 - \frac{\Delta t}{2\tau_{\rm LB}}\right)\omega_i\left[\frac{\boldsymbol{c}_i - \boldsymbol{U}}{c_{\rm s}^2} + \left(\frac{\boldsymbol{U}\cdot\boldsymbol{c}_i}{c_{\rm s}^4}\right)\boldsymbol{c}_i\right]\cdot\boldsymbol{F} \ . \tag{6}$$

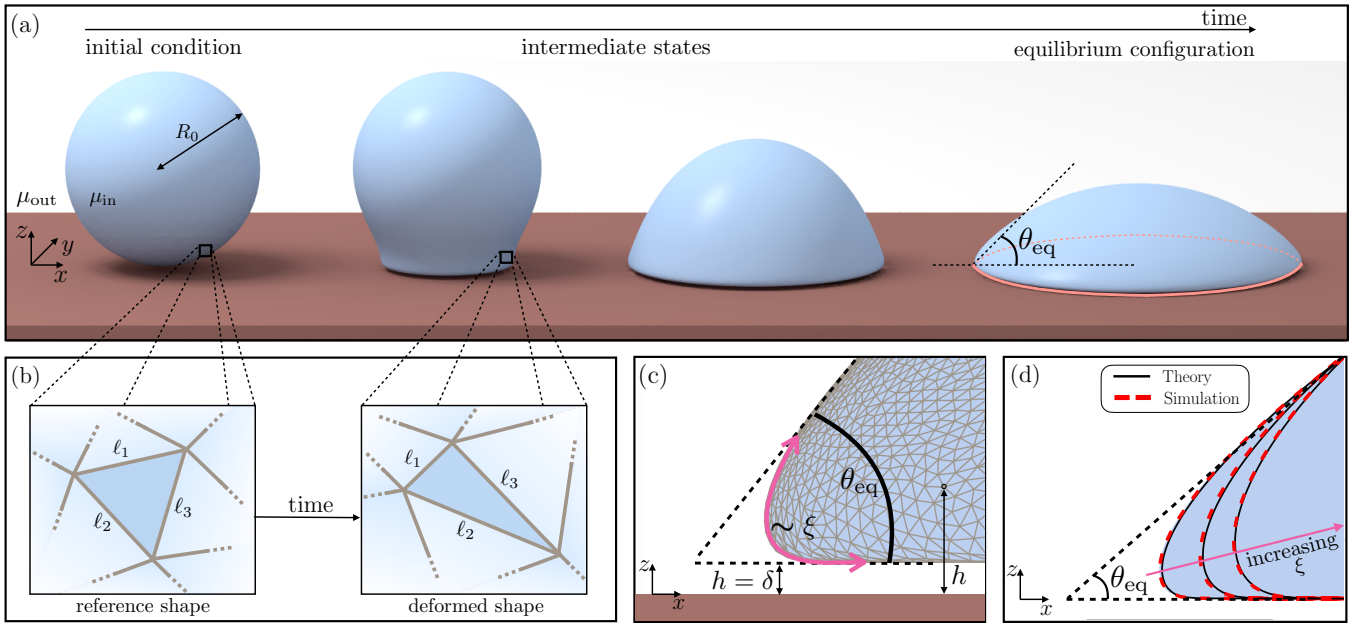

FIG. 1. A sketch describing simulations of a droplet spreading on a flat substrate with the immersed boundary (IB) - lattice Boltzmann (LB) numerical method. Panel (a): macroscopic view of the spreading process allowing an initially spherical droplet with radius R_0 to attain its equilibrium configuration with contact angle θ_{eq}. The droplet interface features a 3D triangular mesh that evolves in time [panel (b)] due to the action of surface tension and wetting forces [cf. Eq. (14)]. The interface is further coupled (via the IB technique) with the dynamics of Newtonian viscous fluids (obtained with the LB technique) outside and inside the droplet, featuring dynamic viscosities μ_{out} and $\mu_{in} = \lambda\mu_{out}$ respectively [cf. Eq. (9)]. Panel (c): mesoscale regularization of the interface profile close to the contact line set by the wall-interaction term $\Pi(h)$, with h the vertical distance of the interface from the wall [cf. Eq. (26)]. The change of the interface curvature from the outer region (spherical cap with contact angle θ_{eq}) to the inner region (thin film with thickness δ) is regulated by the lengthscale ξ, with increasing ξ accommodating more gentle curvature changes [panel (d), see text for more details]. The static profiles are also controlled via analytical solutions [continuous lines in panel (d)].

The hydrodynamic variables are recovered by taking the moments of the PDF [38, 54]:

$$\rho(\boldsymbol{x},t) = \sum_i f_i(\boldsymbol{x},t)\,, \tag{7}$$

$$\boldsymbol{U}(\boldsymbol{x},t) = \frac{1}{\rho(\boldsymbol{x},t)}\sum_i \boldsymbol{c}_i f_i(\boldsymbol{x},t) + \frac{\boldsymbol{F}(\boldsymbol{x},t)\Delta t}{2\rho(\boldsymbol{x},t)}\,, \tag{8}$$

where the equation for the fluid velocity $\boldsymbol{U}$ contains the half-force correction [38, 54]. The continuity and the Navier-Stokes equations (cf. Eqs. (1)-(2)) are recovered for the hydrodynamic variables in Eqs. (7)-(8), with dynamic viscosity set by $\mu = \rho c_s^2(\tau_{LB} - \Delta t/2)$, while the pressure is given by $p = c_s^2\rho$. To account for the varying fluid viscosity inside and outside the droplet, we consider the LB relaxation time as a function of both space and time: $\tau_{LB} = \tau_{LB}(\boldsymbol{x},t)$. At each time step, using a ray tracing algorithm already employed in previous works [48, 50, 51], we identify the lattice nodes located inside and outside the closed interface and set them to the values $\tau_{LB} = \tau_{LB}^{in}$ and τ_{LB}^{out}, respectively. Correspondingly, we define the viscosity ratio λ as the ratio between the inner dynamic viscosity $\mu_{in} = \rho c_s^2(\tau_{LB}^{in} - \Delta t/2)$ and the outer one $\mu_{out} = \rho c_s^2(\tau_{LB}^{out} - \Delta t/2)$:

$$\lambda = \frac{\mu_{in}}{\mu_{out}}. \tag{9}$$

To model the droplet interface, we introduce a set of Lagrangian nodes arranged in a 3D triangular mesh (see Fig. 1), corresponding to a number of N_t triangles. The positions of the nodes, $\boldsymbol{q}_j(t)$ ($j = 1,\ldots,N$, where N is the number of nodes), change over time following the droplet motion. While our implementation does not currently support topology changes – required to simulate drop coalescence or breakup – we emphasize that this is not an intrinsic limitation of the method [55–58]. This feature has not yet been implemented as it is not required for the purpose of this study. The interaction between the fluid and the droplet interface relies on a two-way coupling between the Eulerian lattice and the Lagrangian nodes: at every time step, nodal forces $\boldsymbol{\varphi}_j$ are evaluated on every mesh node and spread onto the fluid nodes to obtain the local force density $\boldsymbol{F}$; at the same time, a no-slip condition is enforced by requiring the velocity of the Lagrangian nodes, $\dot{\boldsymbol{q}}_j(t)$, to match the surrounding fluid velocity $\boldsymbol{U}$. The fluid-structure coupling is then obtained

as:

$$\boldsymbol{F}(\boldsymbol{x},t)=\sum_j \boldsymbol{\varphi}_j(t)\Delta(\boldsymbol{q}_j(t)-\boldsymbol{x})\ , \tag{10}$$

$$\dot{\boldsymbol{q}}_j(t)=\sum_{\boldsymbol{x}} \boldsymbol{U}(\boldsymbol{x},t)\Delta(\boldsymbol{q}_j(t)-\boldsymbol{x})\Delta x^3\,. \tag{11}$$

The above discretized integrals are implemented by using a four-point interpolation stencil, encoding a discrete approximation of the Dirac delta function $\delta(\boldsymbol{x})$ as $\Delta(\boldsymbol{x}) \coloneqq \Psi(x)\Psi(y)\Psi(z)/\Delta x^3$, where $\Psi(x)$ is given by [38]

$$\Psi(x)=\begin{cases}\frac{3}{8}-\frac{1}{4}\frac{|x|}{\Delta x}+\frac{1}{4}\sqrt{\frac{|x|}{\Delta x}-\frac{x^2}{\Delta x^2}+\frac{1}{4}}, & \frac{|x|}{\Delta x}\le 1\\ \frac{5}{8}-\frac{1}{4}\frac{|x|}{\Delta x}-\frac{1}{4}\sqrt{3\frac{|x|}{\Delta x}-\frac{x^2}{\Delta x^2}-\frac{7}{4}}, & 1\le\frac{|x|}{\Delta x}\le 2\\ 0, & \frac{|x|}{\Delta x}\ge 2\end{cases} \tag{12}$$

and, analogously, for $\Psi(y)$ and $\Psi(z)$. Finally, at every time step, the positions of the Lagrangian nodes are updated using a single-step forward Euler scheme:

$$\boldsymbol{q}_j(t+\Delta t)=\boldsymbol{q}_j(t)+\dot{\boldsymbol{q}}_j(t)\Delta t\,. \tag{13}$$

Surface tension and wettability forces are encoded in the force density $\boldsymbol{F}$ (see Eq. (2)) which is localized at the interface. Thus, we split its contributions into two parts: a surface tension force ($\boldsymbol{F}_\sigma$) and a wetting force ($\boldsymbol{F}_\Pi$). In formulas, this means that:

$$\begin{aligned}\boldsymbol{F}(\boldsymbol{x},t)&=\left[\boldsymbol{F}_\sigma+\boldsymbol{F}_\Pi\right]\delta(\boldsymbol{x}-\boldsymbol{r})=\\ &=-\left[\sigma\hat{\boldsymbol{n}}\left(\boldsymbol{\nabla}\cdot\hat{\boldsymbol{n}}\right)+\Pi(h)\hat{\boldsymbol{n}}\right]\delta(\boldsymbol{x}-\boldsymbol{r})\end{aligned} \tag{14}$$

where $\hat{\boldsymbol{n}}$ is the normal at the interface pointing out of the droplet, and $\Pi(h)$ represents an interaction term that depends on the distance h of the interface node from the wall [see Fig. 1(c)]. The latter represents an important computational ingredient of this work, since it controls the droplet wettability. Its implementation, whose details are provided in Sec. II C, marks a key distinction from the approach in Ref. [28], where the wetting dynamics is driven by a Lennard–Jones force orthogonally-oriented with respect to the wall. By adopting Eq. (14) and employing a proper definition of the interaction term $\Pi(h)$ (see Sec. II C), we overcome the limitations reported in Ref. [28] regarding the impossibility to achieve small contact angles. As discussed below, Eq. (14) provides greater analytical control over the solution. In the following sections, we report details on how the surface tension is implemented in our model and on the choice of the interaction term $\Pi(h)$.

B. Modelling surface tension forces

To simulate a droplet with a given surface tension σ, we follow the approach presented in Ref. [28] and rely on consolidated results from elasticity theory [59–61], here briefly reviewed. Let $\boldsymbol{X}(t)$ be the position of a surface element, and $\boldsymbol{X}_0$ the position of the same element in some reference configuration (e.g., in the configuration at rest). The deformation gradient tensor is given by:

$$\boldsymbol{C}(t)=\frac{\partial \boldsymbol{X}(t)}{\partial \boldsymbol{X}_0}\ . \tag{15}$$

Since we are interested in interfacial modeling, we consider the following projection onto the surface of the droplet:

$$\boldsymbol{D}(t)=\boldsymbol{P}(t)\cdot\boldsymbol{C}(t)\cdot\boldsymbol{P}(t=0)\ , \tag{16}$$

where $\boldsymbol{P}(t)=[\mathbb{1}-\hat{\boldsymbol{n}}(t)\otimes\hat{\boldsymbol{n}}(t)]$ is a projection operator, with $\mathbb{1}$ being the 3D identity tensor [60]. One can define two strain invariants starting from $\boldsymbol{D}$, i.e.,

$$a=\frac{1}{2}\log\left\{\frac{1}{2}\left[\mathrm{tr}(\boldsymbol{D}\cdot\boldsymbol{D}^T)\right]^2-\frac{1}{2}\mathrm{tr}\left[(\boldsymbol{D}\cdot\boldsymbol{D}^T)^2\right]\right\}\ , \tag{17a}$$

$$b=\frac{1}{2}\mathrm{tr}(\boldsymbol{D}\cdot\boldsymbol{D}^T)-1\ , \tag{17b}$$

that can be used to write the interface stress $\boldsymbol{\Sigma}$ and the force $\boldsymbol{F}_\sigma$ exerted by the interface [60]:

$$\boldsymbol{\Sigma}=e^{-a}\left[\frac{\partial w}{\partial a}\boldsymbol{P}(t)+\frac{\partial w}{\partial b}\boldsymbol{D}\cdot\boldsymbol{D}^T\right]\ , \tag{18}$$

$$\begin{aligned}\boldsymbol{F}_\sigma=\boldsymbol{P}\cdot\boldsymbol{\nabla}\cdot\boldsymbol{\Sigma}=&-e^{-a}\left(\frac{\partial w}{\partial a}+\frac{\partial w}{\partial b}\right)\hat{\boldsymbol{n}}\boldsymbol{\nabla}\cdot\hat{\boldsymbol{n}}+\\ &+\boldsymbol{P}\cdot\boldsymbol{\nabla}\left[e^{-a}\left(\frac{\partial w}{\partial a}+\frac{\partial w}{\partial b}\right)\right]+\\ &+\boldsymbol{P}\cdot\boldsymbol{\nabla}\cdot\left[e^{-a}\frac{\partial w}{\partial b}(\boldsymbol{D}\cdot\boldsymbol{D}^T-\mathbb{1})\cdot(\mathbb{1}-\hat{\boldsymbol{n}}\otimes\hat{\boldsymbol{n}})\right]\ ,\end{aligned} \tag{19}$$

with w being the strain energy function that characterizes the mechanical response of the interface. We can recognise the surface tension coefficient σ in the first term of Eq. (19) as

$$\sigma\equiv e^{-a}\left(\frac{\partial w}{\partial a}+\frac{\partial w}{\partial b}\right)\ . \tag{20}$$

As shown in Ref. [60], one can choose the strain energy for a droplet with surface tension σ, such that $e^{-a}\frac{\partial w}{\partial a}=\sigma$ and $\frac{\partial w}{\partial b}=0$, thus obtaining:

$$w(a)=\sigma e^a\ . \tag{21}$$

Eq. (19) therefore becomes:

$$\boldsymbol{F}_\sigma=-\sigma\hat{\boldsymbol{n}}(\boldsymbol{\nabla}\cdot\hat{\boldsymbol{n}}). \tag{22}$$

Note that the second term of Eq. (19) is zero because σ is constant. We remark that the force in Eq. (19) is defined and computed at the droplet interface before being spread to the fluid via the IB-LB coupling described in the previous section, hence resulting in the first term of the right-hand side of Eq. (14). The numerical implementation of the surface tension force follows finite-element-method-like technique whose details, found in Ref. [62], are here briefly sketched. On each triangle of the triangulated mesh, whose vertices' positions are $\boldsymbol{q}_{1,2,3}(t)$, we define the displacement vectors, $\boldsymbol{V}_{1,2,3}(t)=\boldsymbol{q}_{1,2,3}(t)-\boldsymbol{q}_{1,2,3}(t=0)$, which are used to compute the displacement:

$$\boldsymbol{V}(t)=N_1\boldsymbol{V}_1+N_2\boldsymbol{V}_2+N_3\boldsymbol{V}_3\ , \tag{23}$$

with $N_{1,2,3}(x,y)=a_{1,2,3}x+b_{1,2,3}y+c_{1,2,3}$ being the shape functions and whose coefficients are reported in Ref. [62]. Eq. (23) can be used to formulate the discrete version of Eq. (16):

$$\boldsymbol{\mathcal{D}}(t)=\boldsymbol{I}+\boldsymbol{\nabla}\boldsymbol{V}(t)\ , \tag{24}$$

where $\boldsymbol{\nabla}\boldsymbol{V}$ is a 2D second-rank tensor, and $\boldsymbol{I}$ is the 2D identity tensor. We then use $\boldsymbol{\mathcal{D}}$ to compute the strain invariants on each triangle (see Eqs. (17)), which are used to evaluate

the strain energy w [see Eq. (21)]. Finally, the contribution to the force density on each node of the mesh given by the surface tension at the interface is:

$$\boldsymbol{\varphi}_{\sigma,j} = -\frac{\partial w}{\partial \boldsymbol{V}_j} \ . \tag{25}$$

C. Modelling wetting properties

Earlier studies [63] used the IB approach to investigate dynamic contact angles on surfaces with complex wettability. In that approach, the contact angle is explicitly imposed as a boundary condition, which enables the treatment of surfaces with complex features. However, it requires the use of interface normals, which is particularly challenging near boundaries. In contrast, in our LB implementation of wetting properties, we avoid challenges associated with accurately defining the interface normals near solid boundaries, and we regularize the interface curvature in such a way that the desired contact angle emerges as the large-scale limit of some inner mesoscale interaction model. This is achieved via the introduction of the interaction term $\Pi(h)$ in Eq. (14) as follows [26, 64, 65]

$$\Pi(h) = A\left[\left(\frac{\xi}{h}\right)^n - \left(\frac{\xi}{h}\right)^m\right] \ , \tag{26}$$

where n and m ($n > m$) are parameters regulating the effective range of the interaction, A is constant, and h measures the (vertical) distance from the solid surface [see Fig. 1(c)]. It is worth noting that a film with thickness δ develops below the droplet, with the property $\delta \to 0$ as $\xi \to 0$ (see Appendix C). The *regularizing lengthscale* ξ is tunable in the model and sets the characteristic lengthscale that regulates interface curvature changes when the outer interface profile approaches solid walls [see Fig. 1(c)]. Regarding the numerical implementation, the interaction term $\Pi(h)$ is computed on each Lagrangian node of the mesh representing the interface. For each node j, we calculate the corresponding wetting nodal force, $\boldsymbol{\varphi}_{\Pi,j}$, which contributes to the IB method [see Eq. (10)] as

$$\boldsymbol{\varphi}_{\Pi,j} = -\frac{\chi_j}{3}\Pi(h)\hat{\boldsymbol{n}}_j \ , \tag{27}$$

where $\hat{\boldsymbol{n}}_j$ is taken as the average of the normal vectors of all faces that share the j-th node, while χ_j represents the area of the mesh associated with the j-th node. The factor $1/3$ accounts for each triangle area being shared by three vertices. This renormalization using the nodal area is necessary to ensure robustness to mesh discretization. Similar to the surface tension forces, the wetting force is spread to the fluid via the IB method, resulting in the second term of the right-hand side of Eq. (14). Let us now discuss the choice of the parameters m, n, A, and ξ of the wall-interaction force. From the balance between the surface tension forces with the wetting forces at the interface one obtains

$$\Delta p = \sigma\, \boldsymbol{\nabla}\cdot\hat{\boldsymbol{n}} + \Pi(h) \ , \tag{28}$$

where Δp is the pressure jump across the droplet interface. In Appendix A, we show that the interface profile displays a wedge-like structure near the wall, which becomes more prominent as the micro-scale ξ becomes much smaller than the droplet radius, R_0, noting that the infinite, wedge-like assumption becomes less relevant for smaller contact angles (see Appendix C). This wedge is characterized by an angle $\theta_{\rm eq}$, which is related to σ, A, n, and m as follows [26, 64, 65]:

$$A = \sigma\frac{(m-1)(n-1)}{(n-m)\xi}(1+\cos\theta_{\rm eq}). \tag{29}$$

Eq. (29) allows a controlled use of the parameters A, m, n, and ξ with a precise link with the equilibrium contact angle $\theta_{\rm eq}$, without the need of any pre-calibration step on model parameters, as done in Ref. [28]. Moreover, as discussed in detail in the next section [see also Fig. 1(d)], for a given θ_{eq}, the lengthscale ξ can be further used to achieve the desired level of interface profile regularization close to the contact line.

The use of the wall-interaction force of the form given in Eq. (26) echoes the disjoining-pressure term which is commonly invoked to account for the inter-molecular interactions of thin films near a substrate [66], allowing the formation of a thin pre-wetting film ahead of the contact line in pseudo-partial wetting scenarios [2, 67, 68]. Here, as in relevant works in the literature [26, 64, 65, 69], the Lennard–Jones-like interaction term $\Pi(h)$ is used to model strong repulsions at short distances between the droplet and the substrate, and attraction at intermediate distances. In this manner, $\Pi(h)$ primarily impacts the contact angle and the shape of the interface near the substrate. Importantly, its presence regularizes the curvature of the droplet interface, suppressing any stresses that would have resulted in the vicinity of a moving contact line. Indeed, dealing with abrupt curvature changes would introduce strongly localized forces in the interface model, which, in turn, could cause numerical instabilities when the interface is coupled with the fluid via the IB method (see Sec. II A) [38]. We emphasize that our approach in modeling wetting is not primarily aimed at establishing a precise link between $\Pi(h)$ and the underlying molecular physics. Indeed, the nanoscale effects, which would significantly impact the value of the surface forces (and hence the contact angle) in the area surrounding the droplet [3], are not physically represented within the proposed approach. Instead, we utilize an efficient and straightforward computational strategy (inspired by physics) that allows smooth curvature changes over the lengthscale ξ near the contact line. The method is then meant to be used in the limit $\xi/R_0 \to 0$, where we will show that relevant macroscopic features of wetting are reproduced via quantitative benchmarks and model validations, both for droplet statics (see Sec. III A) and spreading (see Sec. III B). We finally remark that as $\xi/R_0 \to 0$, the thickness of the thin film that develops below the droplet becomes vanishingly small [see Appendix C; see also Fig. 1(c)], but still prevents direct contact of the interface nodes with the wall. Furthermore, as demonstrated in earlier literature papers [65], the model can also be equipped with a boundary condition (not implemented in the present study) for the tangential stress if adhesion properties with the wall are desired. In other words, in the limit $\xi/R_0 \to 0$, the model is flexible enough to avoid "floating" droplet-like configurations.

III. NUMERICAL RESULTS

In this section, we discuss numerical simulation results to validate the implementation of the IB-LB model. First, we consider the droplet at equilibrium and compare the droplet's shape obtained from numerical simulations with the

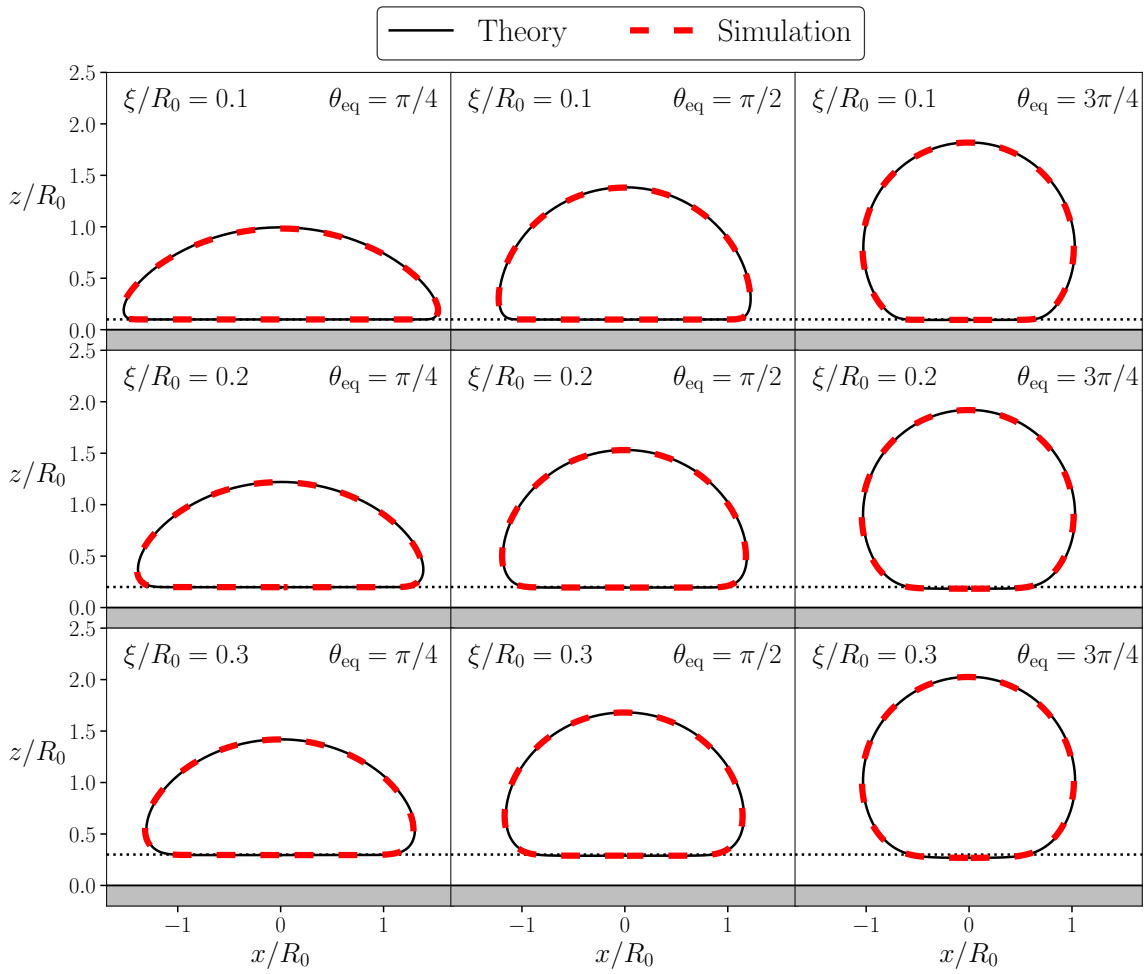

FIG. 2. Comparison of droplet profiles at equilibrium between the equilibrium solution obtained by solving Eq. (28) (solid black lines) and the simulated results (dashed red lines) for different combinations of equilibrium contact angle, θ_{eq} and normalized regularization lengthscale ξ/R_0 (different panels): θ_{eq} increases from left to right, while ξ/R_0 increases from top to bottom. The dotted line represents the height $z/R_0 = \xi/R_0$ [see Eq. (26)].

corresponding theoretical prediction (Sec. III A). Then, in Sec. III B, we consider the spreading dynamics of the droplet towards equilibrium shapes.

The numerical simulations have been carried out in a 3D domain, with edges of length L_x, L_y, and L_z. In all simulations, we set $\Delta x = \Delta t = 1$, hence they will be dropped hereafter. The boundary conditions are taken to be periodic along the x and y directions [see Fig. 1] while the no-slip boundary condition is enforced at the top and bottom boundaries using a bounce-back approach [38]. Throughout this work, the initial density was always set to unity and the exponents in Eq. (26) were taken to be $(n, m) = (6, 3)$ as attested in related studies [70, 71]. Simulations ran on NVIDIA Ampere A100 64GB graphics processing units (GPUs), with a simulation time for each spreading process lasting between 0.5 and 12 hours, depending on simulation parameters. In a typical simulation with $L_x = L_y = L_z = 64$ and a triangular mesh with $N_t = 5 \times 10^5$ faces, we achieve approximately 50 mega lattice-updates per second (MLUPS).

A. Statics

We started our investigations by analyzing the droplet shapes in equilibrium conditions. Numerical simulations were performed in a box of dimension $L_x \times L_y \times L_z = 80 \times 80 \times 60$. To reach equilibrium, we start with an equilibrated spherical droplet, with initial radius $R_0 = 20$ modelled with $N_t = 40\,000$ triangles, which is placed close to the substrate, at a distance where the interaction term $\Pi(h)$ is non-negligible. This way, the droplet starts to spread [see Fig. 1(a)] until the equilibrium state is achieved. The viscosity ratio between the inner and outer phases is $\lambda = 1$. We considered different equilibrium contact angles, $\theta_{eq} \in \{\pi/4,\ \pi/2,\ 3\pi/4\}$, and different values of the normalized regularization lengthscale, $\xi/R_0 \in \{0.1, 0.2, 0.3\}$.

The equilibrium droplet shape is extracted from numerical simulations and compared with analytical predictions. In particular, under the assumption of an axisymmetric droplet, one can derive a differential equation for the profile of the surface of the droplet, which is described in spherical coordinates in terms of the radial distance from the origin with a profile

of the form $r = G(\phi)$, with ϕ being the polar angle formed with the z-axis. For a schematic, derivation and implementation details of the differential equation for the droplet shape [Eq. (28)], see Appendix B; for further commentary on its asymptotic structure see Appendix C.

In Fig. 2, we report a comparison between the theoretical droplet shape obtained by solving Eq. (28) (solid black lines) and the simulated ones (dashed red lines) extracted by taking a slice over a plane orthogonal to the y-axis and passing through the droplet's center of mass. Overall, the agreement between the simulated droplet shapes and the theoretical predictions is excellent for all combinations of ξ/R_0 and $\theta_{\rm eq}$. To delve deeper into the matter, we computed the error between the theoretical radial profile $G_{\rm theo}(\phi)$ and the simulated one $G_{\rm sim}(\phi)$ by averaging on the azimuthal angle ϕ:

$$\mathrm{E_{L_2}} = \sqrt{\frac{\int_0^\pi |G_{\rm sim}(\phi) - G_{\rm theo}(\phi)|^2 \mathrm{d}\phi}{\int_0^\pi |G_{\rm theo}(\phi)|^2 \mathrm{d}\phi}}\,. \tag{30}$$

Here, the integration domain is restricted to $\phi \in [0, \pi]$ because of the axial symmetry of the problem. Fig. 3 shows the error $\mathrm{E_{L_2}}$ as a function of ξ/R_0 for different values of $\theta_{\rm eq}$. There, $G_{\rm sim}(\phi)$ is extracted by considering the radial distance of every Lagrangian node from the droplet's centroid. The radius R_0 is kept fixed to $R_0 = 20$. To evaluate the influence of interface resolution, we performed numerical simulations with different numbers of triangles: $N_t = 20\,000$ [Fig. 3(a)] and $N_t = 40\,000$ [Fig. 3(b)]. In Fig. 3(a), the error $\mathrm{E_{L_2}}$ is generally small, decreasing to approximately 0.001 as ξ/R_0 increases. For the largest value of the equilibrium contact angle ($\theta_{\rm eq} = 3\pi/4$), the error is independent of ξ/R_0. Conversely, for smaller values of $\theta_{\rm eq}$, the error increases as ξ/R_0 decreases, becoming pronounced around a critical value $(\xi/R_0)^*$. The critical value $(\xi/R_0)^*$ is larger for smaller values of $\theta_{\rm eq}$: for $\theta_{\rm eq} = \pi/4$, the error reaches a peak value of approximately $\mathrm{E_{L_2}^{peak}} \simeq 0.1$. These effects are likely tied to the discretization of the droplet interface. By comparing Fig. 3(a) and Fig. 3(b), it is clear that higher resolution leads to a transition to smaller errors occurring at lower values of $(\xi/R_0)^*$. Additionally, the peak error, $\mathrm{E_{L_2}^{peak}}$, is reduced for smaller values of $\theta_{\rm eq}$ when a finer discretization is used. Such a resolution study reveals that $N_t = 40\,000$ provides a good resolution, as the maximum error is found to be $\mathrm{E_{L_2}^{peak}} \simeq 0.01$ for the smallest $\theta_{\rm eq}$ considered. In contrast, $N_t = 20\,000$ does not achieve good convergence, as evidenced by higher errors and oscillations for small values of ξ/R_0. We therefore performed all simulations for the statics with $N_t = 40\,000$.

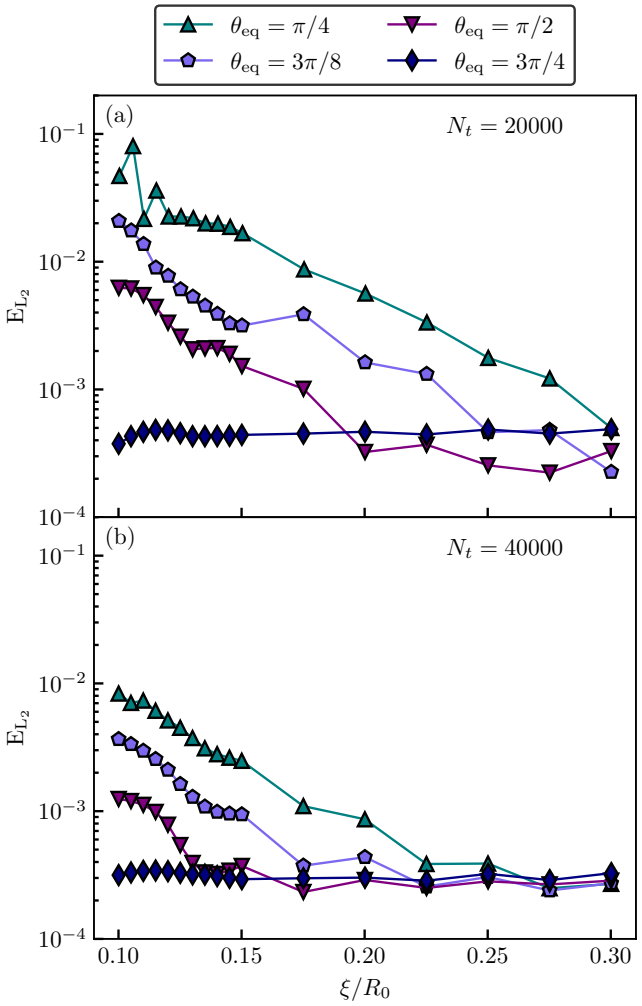

FIG. 3. Error $\mathrm{E_{L_2}}$ between IB-LB simulations and theoretical prediction (cf. Eq. (30)) as a function of the normalized regularization lengthscale, ξ/R_0, for different values of θ_{eq} (different symbols/colors). We consider different realizations for the number of triangles on the droplet interface: $N_t = 20\,000$ (top panel) and $N_t = 40\,000$ (bottom panel).

B. Dynamics

In this section, we report on results of numerical simulations for the spreading dynamics of a droplet on a flat surface. The process of droplet spreading is characterized by different regimes, where different force contributions balance and produce different scaling laws for the evolution of the contact radius $r_c(t)$, i.e., the radius of the interface area that is in contact with the wall. The initial stages of spreading have been investigated in several experimental, numerical and theoretical works [9, 17, 18, 20–23, 72–79]. If Laplace pressure balances the inertial terms, an inertial scaling regime is expected, for which $r_c(t) \sim t^{1/2}$, echoing the inertial scaling of the contact area between two coalescing droplets [80–86]. This inertial scaling is verified in spreading experiments on completely wetting surfaces as well as in the initial stages of spreading of droplets on partially wetting surfaces, while for later stages a departure from the 1/2 exponent is observed [72–75].

In the very late stage of spreading dynamics, a much slower process is expected, when viscous effects balance surface tension forces, reproducing the celebrated Tanner's law, $r_c(t) \sim t^{1/10}$ [3, 87, 88]. Since the wetting modeling implemented in our IB-LB method (see Sec. II C) does not result in a direct contact between the interface and the wall, it is natural to look for an appropriate definition of the contact radius $r_c(t)$. For this reason, we first investigate the sensitivity of the expected scaling laws to the way $r_c(t)$ is defined. With this aim, we design two protocols to determine the contact radius: (*i*) following an earlier work on the subject [89], we identify the contact line as the intersection between the droplet interface and a plane parallel to the wall placed at the height $z_{\rm cut}$, referred to as the *intersection parameter*; then, we evaluate the

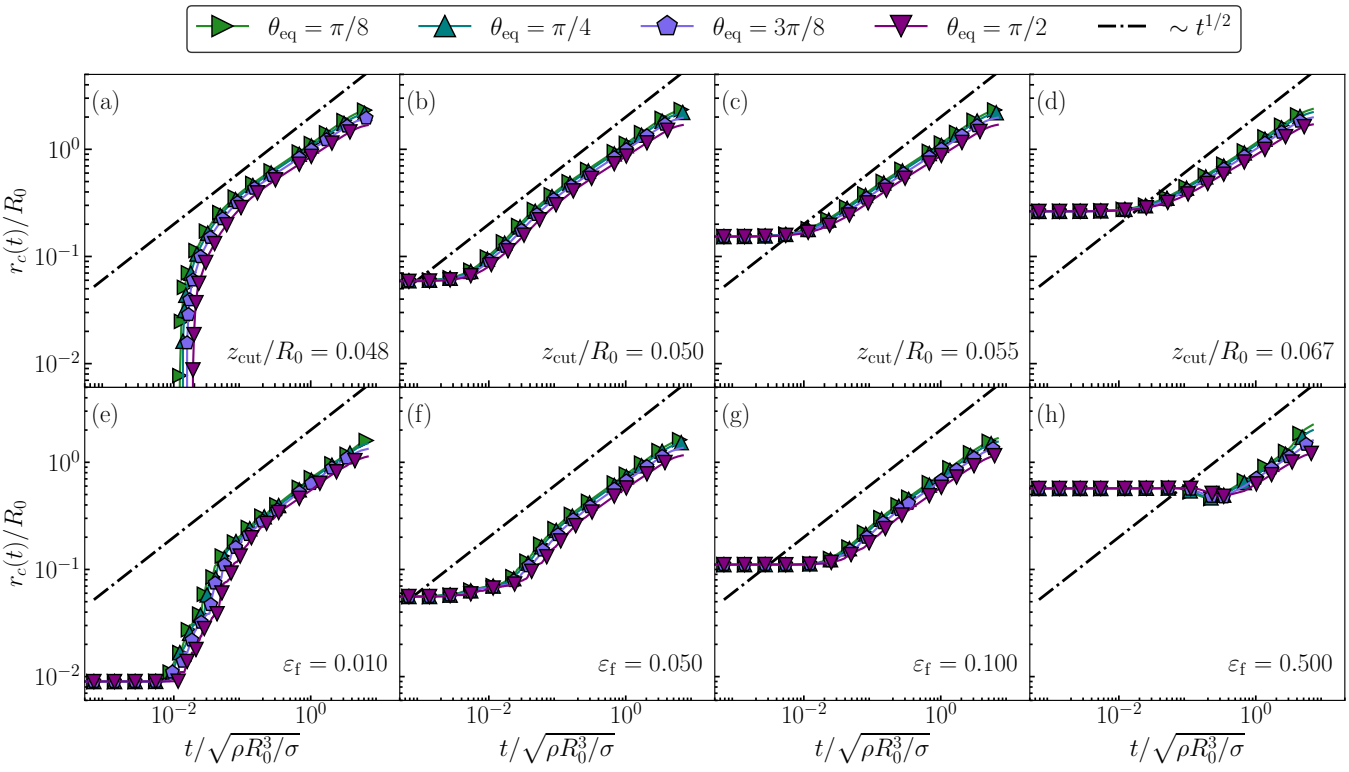

FIG. 4. Droplet contact radius $r_c(t)$ as a function of time in the early stages of spreading dynamics, normalized with respect to the initial droplet radius R_0, for different equilibrium contact angles θ_{eq} (different colors/symbols). Reported time is normalized with respect to the characteristic inertial timescale $\tilde{t} = \sqrt{\rho R_0^3/\sigma}$. To determine the proper definition of the contact radius, we compare the spreading dynamics for two definition protocols (see text for more details): top panels refer to protocol (*i*), based on the intersection parameter z_{cut}, and show results for different values of z_{cut}/R_0; bottom panels refer to protocol (*ii*), based on the flatness parameter ε_f, and show results for different values of ε_f.

contact radius as the average distance of the contact line from the center of the contact region at height z_{cut}; (*ii*) we consider the portion of the droplet interface that forms a flat region parallel to the wall: since the droplet surface is discretized into triangles, one has to focus on the lower half of the droplet and consider each triangular element individually. A triangle, whose vertices are positioned at $\boldsymbol{q}_i$ (see Sec. II A), is included as part of the flat region if $\max_{i,j} |(\boldsymbol{q}_i - \boldsymbol{q}_j) \cdot \hat{\boldsymbol{n}}_w| < \varepsilon_f R_0$, where the indices i and j run on the three vertices of the triangle, $\hat{\boldsymbol{n}}_w$ is the unit normal to the wall, and ε_f is a threshold parameter, referred to as the *flatness parameter*. The contact area computed using this procedure (χ_{ε_f}) is determined as the sum of the areas of all triangles that satisfy the flatness criterion. The corresponding contact radius, r_{ε_f}, is then calculated by assuming that χ_{ε_f} corresponds to the area of a circle with radius r_{ε_f}.

We first focus on the dynamics in the early stages of wetting, where an inertial scaling law $r_c(t) \sim t^{1/2}$ is expected for the contact radius $r_c(t)$. By using protocols (*i*) and (*ii*) and comparing against the expected scaling law, we assess the robustness in measuring $r_c(t)$ as the free parameters z_{cut} and ε_f are varied. This is done by performing dedicated simulations with $\xi = 2$, and $\lambda = 10$ in a domain of size $L_x \times L_y \times L_z = 240 \times 240 \times 130$. Simulations are initialized as described in Sec. III A, with a spherical droplet of radius $R_0 = 60$ initially placed close to the wall, at distances where the wall-interaction force is not negligible in order to enable spreading. Notice that we chose a value of R_0 larger than the ones used for the static simulations to achieve a smaller Ohnesorge number, $\mathrm{Oh} = \mu/(\rho R_0 \sigma)^{1/2}$, and facilitate comparisons with literature results. In Fig. 4, we analyze the time evolution of the contact radius $r_c(t)$ for both protocols (*i*) and (*ii*). The reported time is normalized with the inertial timescale $\tilde{t} = \sqrt{\rho R_0^3/\sigma}$ [21, 26, 73, 75]. Figures 4(a)-(d) refer to protocol (*i*) and show different values of the normalised intersection parameter z_{cut}/R_0, while Figs. 4(e)-(h) report results obtained by employing protocol (*ii*) for different values of the flatness parameter ε_f. Different symbols/colors correspond to different values of the equilibrium contact angles θ_{eq}. The inertial scaling $r_c(t) \sim t^{1/2}$ is also reported for comparison. As expected, varying the parameter that pertains to each protocol has a non-trivial impact on the measured radius, particularly at early stages when the contact radius is small. For protocol (*i*), a plateau is seen until the points on the contact plane, fixed at the height z_{cut} from the wall, are unaffected by the spreading process. For protocol (*ii*), a larger value of ε_f means a triangle is considered flat with a lower tolerance; therefore, the region judged as flat is constant for a longer period. Then, when the contact radius starts to increase, it soon approaches an inertial-like scaling

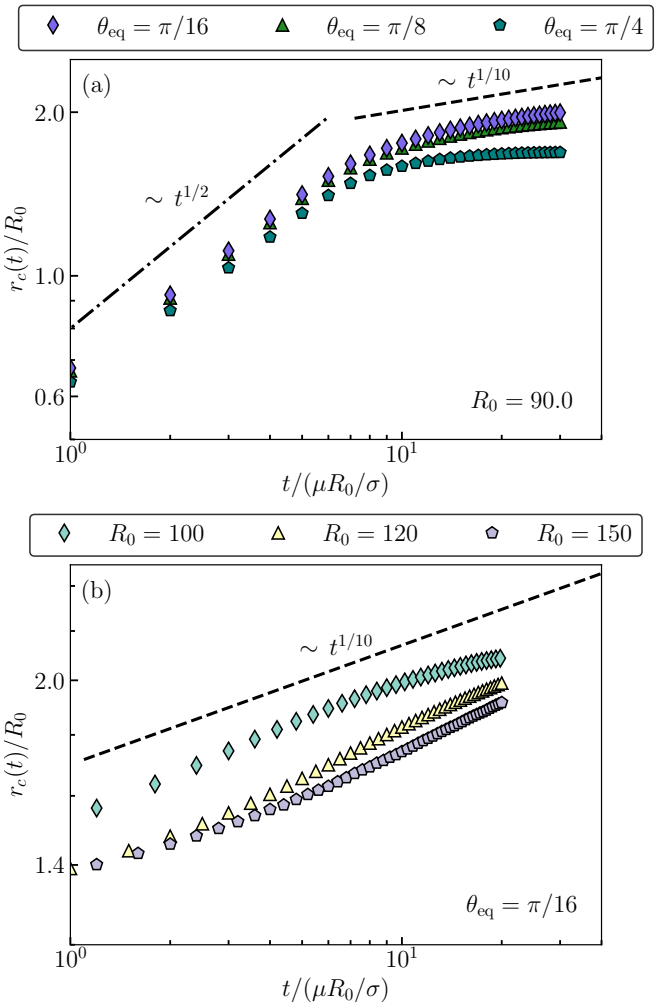

FIG. 5. Dynamics of the droplet contact radius $r_c(t)$ at early and late stages of spreading. Contact radius is normalized with respect to initial droplet radius R_0. Time is normalized with respect to characteristic viscous time t^*. Top panel: evolution of $r_c(t)$ for different values of the equilibrium contact angle θ_{eq} (different colors/symbols) based on simulations with $R_0 = 90$; scaling laws for inertial regime (dash-dotted line) and viscous regime (dashed line) are also reported. Bottom panel: evolution of the contact radius for a fixed contact angle ($\theta_{eq} = \pi/16$) and different values of R_0 (different colors/symbols) based on simulations where the droplet is initialized as a spherical cap; dashed line refers to the scaling law for viscous regime.

with a power-law behavior very close to $r_c(t) \sim t^{1/2}$: this happens for all the considered values of z_{cut} and ε_f, although its onset occurs at different times depending on the values of the two parameters. The earliest onsets for the two protocols is seen in Fig. 4(b) and Fig. 4(f), where it occurs around $t/\tilde{t} \sim 0.01$, with the plateau for protocol (*i*) [panel (b)] lasting slightly less than the plateau for protocol (*ii*) [panel (f)]. Furthermore, it emerges that there exist optimal values of $z_{cut}/R_0 \approx 0.050$ and $\varepsilon_f \approx 0.1$ for which one can get closer to the inertial scaling, showing a nice agreement with molecular dynamics results reported in Ref. [75]. Interestingly, the optimal value of z_{cut} matches the height where we expect to have the maximum curvature for the droplet interface at equilibrium, which roughly occurs at the minimum of the wetting interaction term $\Pi(h = h^*)$, where $h^* = \xi(n/m)^{1/(n-m)}$. For the chosen values of m, n, and ξ, this leads to $h^*/R_0 \approx 0.050$. Regarding the precise details of the power-laws observed, although the corresponding exponents may be fitted [26], visual inspection reveals they are essentially very close to 1/2. Some slight dependence on wettability is observed, especially for the larger values of $r_c(t)/R_0$, with data for smaller θ_{eq} lying slightly above data with larger θ_{eq}, in agreement with the literature [26, 73, 75]. Improving the quality of data below $r_c(t)/R_0 = 0.01$ would probably require larger resolutions. In summary, the measurement of the contact radius $r_c(t)$ sensibly depends on the specific values of the parameter involved in the protocol used. Moreover, there exists an optimal value of the parameter for which the agreement with the expected scaling law is maximized. Although in Fig. 4 it emerges that the choice of the protocol does not markedly impact the optimal agreement with theory, protocol (*i*) could be favored, since it provides a physically intuitive relation that connects the optimal value of the intersection parameter z_{cut} and the height of the maximum curvature.

Next, we investigate the late stage of the dynamics, which is expected to be dominated by viscous forces. In Fig. 5(a), we report results obtained by performing longer simulations with $\xi = 3$, $R_0 = 90$, $N_t = 500\,000$ and different equilibrium contact angles $\theta_{eq} \in \{\pi/16, \pi/8, \pi/4\}$. For larger values of θ_{eq}, the droplet hardly spreads before reaching equilibrium after a brief inertial-spreading stage. For small values of θ_{eq}, however, before the spreading stops, we observe a transition to another scaling close to $r_c(t) \sim t^{1/10}$, as expected from Tanner's law [3, 87, 88], which arises when viscous and surface tension forces prevail. This observation aligns well with previous works [21, 26]. To study the scaling law behavior of the late stage in more detail, we performed additional simulations using a dedicated set-up: the droplet is initialized as a spherical cap, bypassing the initial inertia-dominated spreading process, allowing us to focus directly on the viscous scaling law. Simulations are performed by fixing ξ and using different $R_0 \in \{100, 120, 150\}$ using $N_t = 500\,000$ for the former two radii and $N_t = 750\,000$ for the last one. The results are reported in Fig. 5(b). We observe that, by increasing R_0, the scaling law $r_c(t) \sim t^{1/10}$ is more closely followed, suggesting that a clear separation between the (inner) regularizing lengthscale ξ and the (outer) lengthscale R_0 is necessary to observe Tanner's law. Interestingly, the prefactor is a decreasing function of R_0: when studying viscous spreading modeled using sharp-interface hydrodynamics with a slip length ℓ_s, the predicted prefactor scales like $\sim 1/[\log(R_0/\ell_s)]^{1/10}$. This suggests that, when $R_0/\xi \gg 1$, the mechanism of regularization introduced by the finite lengthscale ξ effectively plays the role of a slip boundary condition on the substrate. More detailed comparisons with the spreading process of a droplet are needed to quantitatively address this point. We finally remark that, during the spreading or retraction process of a droplet, hysteresis effects are present [3], related to the heterogeneities on the substrate that promote the pinning of the contact line. The characteristic size of defects can range from nano/microscopic to macroscopic. Since our method is

a mesoscale one, a precise link with nano/microscale physics is not presently possible. On the other hand, it is possible to generalize the method to include macroscopic defects [65].

IV. CONCLUSIONS

We have studied the statics and dynamics of wetting within the framework of the hybrid immersed boundary - lattice Boltzmann (IB-LB) numerical technique, focusing on the problem of the interaction of a liquid droplet with a solid wall. We leveraged a previous IB-LB model for wetting by some of the authors [28], with the main scope to overcome its limitations related to the difficulty in modeling small contact angles and the need to use pre-calibration simulations to set the desired contact angles. We have substantially extended and improved the method in various directions. We used a controlled implementation of wetting [26, 64, 65] featuring a wall-interaction term $\Pi(h)$ with strong repulsions at short distances and attraction at intermediate distances, thus impacting the profile shape only in the vicinity of the wall. Within this approach, the equilibrium contact angle can be set *a priori* via the suitable choice of the $\Pi(h)$ parameters. Furthermore, a regularization lengthscale ξ is present, which allows to control abrupt curvature changes close to the contact line. We stress that the $\Pi(h)$ term is not meant to be used to model molecular physics; instead, it is used to numerically resolve the dynamics of the contact line preventing a direct contact between the interface nodes and the substrate. The force exerted by the potential is generally weak due to the diminishing effect of Π with distance and as $\xi/R_0 \to 0$. In these limits, we show that the "macroscopic" picture of wetting is well recovered by our mesoscale method, with the static interface shape approaching a wedge-like structure with the desired equilibrium contact angle $\theta_{\rm eq}$. More in detail, analytical predictions for the equilibrium shapes have been successfully verified in simulations; furthermore, we have used simulations to investigate the dynamics of spreading in the inertia-dominated and the viscous-dominated regimes. The results are in agreement with those in the known literature.

Our results pave the way for interesting future developments. First of all, the IB-LB methodology has been widely and successfully used to model complex interface physics, e.g. featuring elasticity and interface viscosity [40–49]. Studying wetting problems involving interface physics with these additional complexities surely poses excellent food for thought in the future perspective. For example, many studies focused on elastic wetting, featuring liquids close to solid walls confined by elastic membranes [30, 31, 33, 35, 36]. The IB-LB model is particularly amenable in accommodating elasticity models at the interface via a suitable change in the constitutive law: this amounts to considering different strain energies in Eq. (19), embedding more information than just surface tension forces; this modeling would probably be more difficult in the context of traditional diffuse interface LB models, such as the pseudopotential LB or the colour gradient models (see Ref. [39] for a recent review). Hence, the IB-LB could be used as an ideal numerical tool to complement experimental observations and/or extend our knowledge on wetting to unexplored settings. Another key noteworthy aspect is the fact that the IB-LB method is particularly efficient; hence, it can be used to generate ground-truth data and explore the possibility of developing data-driven methodologies to unravel the non-linear relation between droplet dynamics and the features that control it [90, 91].

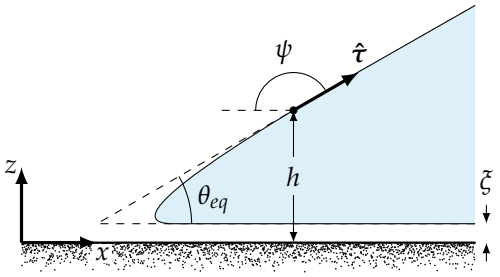

FIG. 6. Wedge-like profile in the limit $\xi/R_0 \to 0$, which is used for obtaining the dependence of A as a function of $\theta_{\rm eq}$.

ACKNOWLEDGMENTS

The authors acknowledge Luca Biferale for insightful preliminary discussions. This research is supported by European Union's HORIZON MSCA Doctoral Networks programme, under Grant Agreement No. 101072344, project AQTIVATE (Advanced computing, QuanTum algorIthms and data-driVen Approaches for science, Technology and Engineering). FP and MS acknowledge the support of the National Center for HPC, Big Data and Quantum Computing, Project CN_00000013 – CUP E83C22003230001 and CUP B93C22000620006, Mission 4 Component 2 Investment 1.4, funded by the European Union - NextGenerationEU. FG acknowledges the support of the Italian Ministry of University and Research (MUR), FARE program (No. R2045J8XAW), project "Smart-HEART". MD benefited from the support of the MediTwin consortium (part of France 2030), Ansys, and from an Inria chair. Funding from the European Union's Horizon 2020 research and innovation programme under grant agreements No. 882340 (European Research Council) and 810660 is also acknowledged.

Appendix A: Setting the wetting interaction strength A

In this section, we provide details on how to relate the constant A in the wetting interaction term in Eq. (26) to the equilibrium contact angle θ_{eq} in the limit of large droplets. At equilibrium ($\boldsymbol{U} = \boldsymbol{0}$), the force balance equation in the normal direction reduces to Eq. (28). For large droplets, the scale ξ is much smaller than the characteristic droplet radius R_0 and we also have $\Delta p \to 0$ as a consequence of the fact that the pressure must be inversely proportional to R_0. Therefore, in the limit when $R_0 \to \infty$, Eq. (28) reduces to $\sigma \boldsymbol{\nabla} \cdot \hat{\boldsymbol{n}} + \Pi(h) \approx 0$ and the free-surface assumes a wedge-like profile in the vicinity of the contact line, whose size allows us to neglect its curvature in the azimuthal direction (see Fig. 6). In this manner, the curvature of the profile may be obtained via the Serret–Frenet formulas [92]

$$\boldsymbol{\nabla} \cdot \hat{\boldsymbol{n}} = \left\| \frac{\mathrm{d}\hat{\boldsymbol{\tau}}}{\mathrm{d}s} \right\| = \frac{\mathrm{d}\psi}{\mathrm{d}s}, \tag{A1}$$

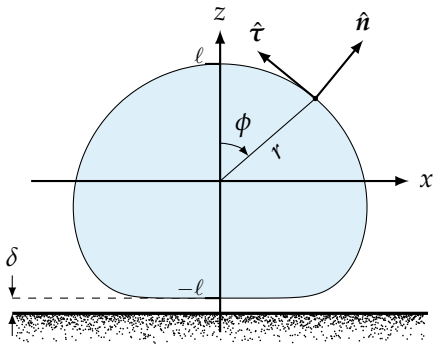

FIG. 7. Droplet geometry. The droplet is centred around the vertical axis and lies at a distance δ above the substrate.

where s is arc length, $\hat{\boldsymbol{\tau}}$ is the tangent vector and ψ is the angle $\hat{\boldsymbol{\tau}}$ makes with the x-axis (see Fig. 6). Since the z-coordinates of the wedge-like profile, $h(s)$, are linked with $\psi(s)$ through $\sin\psi = \mathrm{d}h/\mathrm{d}s$ [93], we may invoke the chain rule to write Eq. (28) in the large-droplet limit as

$$\sigma \sin\psi \frac{\mathrm{d}\psi}{\mathrm{d}h} + \Pi(h) = 0. \tag{A2}$$

To derive Eq. (29), we use the fact that Eq. (A2) is a separable differential equation and we perform integrals over the range h and ψ are defined, namely from $\psi = 0$ [equivalently $h = \xi$ so that Eq. (A2) holds] to $\psi = \pi - \theta_{\mathrm{eq}}$ (equivalently $h \to \infty$, see Fig. 6), so that

$$\sigma \int_0^{\pi-\theta_{\mathrm{eq}}} \sin\psi \,\mathrm{d}\psi = -A \int_\xi^\infty \left[\left(\frac{\xi}{h}\right)^n - \left(\frac{\xi}{h}\right)^m\right] \mathrm{d}h. \tag{A3}$$

The above integrals may be straightforwardly evaluated to yield Eq. (29) [26, 64, 65].

Appendix B: Solving for droplet shapes

In this section, the main ingredients which are necessary to obtain numerical solutions to Eq. (28) are provided. A key step towards this goal is casting the surface profile as a singe-valued function, which is conveniently accomplished by considering the droplet in a spherical coordinate system. Assuming axisymmetry, the radial function identifying the surface is $r = G(\phi)$, where ϕ is the polar angle formed with the z-axis (see Fig. 7). This notation for the polar angle has been decided against the popular choice of θ to avoid notation clash with the contact angle which uses the same variable. The problem is made non-dimensional using $G(\phi) = R_0 g(\phi)$, where, like previously, R_0 is the initial (spherical) droplet radius. This particular form for the droplet profile avoids numerical issues related to the discretization of surfaces of different sizes. The outward unit normal of the surface, $\hat{\boldsymbol{n}}$ is given by

$$\hat{\boldsymbol{n}} = \frac{g}{(g^2+g_\phi^2)^{1/2}}\hat{\boldsymbol{r}} - \frac{g_\phi}{(g^2+g_\phi^2)^{1/2}}\hat{\boldsymbol{\phi}}, \tag{B1}$$

where $\hat{\boldsymbol{r}}$ and $\hat{\boldsymbol{\phi}}$ are the unit vectors in the radial and polar directions, respectively, with subscripts denoting partial differentiation with respect to the denoted variable, ϕ here. Evaluating the divergence of the unit normal in spherical coordinates, we find

$$\boldsymbol{\nabla}\cdot\hat{\boldsymbol{n}} = \frac{2g^2+3g_\phi^2-gg_{\phi\phi}}{R_0(g^2+g_\phi^2)^{3/2}} - \frac{g_\phi\cos\phi}{R_0 g\sin\phi(g^2+g_\phi^2)^{1/2}}. \tag{B2}$$

To facilitate the numerical solution in the vicinity of the polar axes, we notice that $g(\phi)$ is in fact a function of $\cos\phi$. Making the variable change $u = \cos\phi$, Eq. (B2) is cast as an equation for $g(u)$, namely

$$\boldsymbol{\nabla}\cdot\hat{\boldsymbol{n}} = \frac{ug\dot{g}-g^2-(1-u^2)g\ddot{g}}{R_0\left[(1-u^2)\dot{g}^2+g^2\right]^{3/2}} + \frac{u\dot{g}+3g}{R_0 g\sqrt{(1-u^2)\dot{g}^2+g^2}}, \tag{B3}$$

where the dots denote differentiation with respect to $u \in [-1,1]$. The normal force balance equation (28) becomes:

$$k = \frac{ug\dot{g}-g^2-(1-u^2)g\ddot{g}}{\left[(1-u^2)\dot{g}^2+g^2\right]^{3/2}} + \frac{u\dot{g}+3g}{g\sqrt{(1-u^2)\dot{g}^2+g^2}} + R_0\frac{(m-1)(n-1)}{(n-m)\xi}(1+\cos\theta_{\mathrm{eq}})\left[\left(\frac{\xi}{h}\right)^n - \left(\frac{\xi}{h}\right)^m\right], \tag{B4}$$

where we set $k = \Delta p R_0/\sigma$ and h is the distance from the substrate given by $h = R_0\left[ug(u) + g(-1)\right] + \delta$, with $\delta \approx \xi$ being the smallest distance from the substrate which needs to be determined as part of the solution (see Fig. 7). Hence, given k (or equivalently, the volume of the droplet, see below), we determine δ and $g(u)$, subject to

$$g(1) = g(-1), \tag{B5}$$

which means that the origin is placed in the middle between the top and bottom parts of the droplet. Through an integral constraint, we impose the volume of the droplet, which is written as

$$\int_0^\pi g^3(\phi)\sin\phi\,\mathrm{d}\phi = 2, \tag{B6}$$

or, in terms of the u variable, as

$$\int_{-1}^1 g^3(u)\,\mathrm{d}u = 2. \tag{B7}$$

Hence, to determine the droplet profile together with δ and k, we use second-order finite differences to enforce Eq. (B4) everywhere in the domain alongside with conditions Eqs. (B5) and (B7), thus maintaining the same number of degrees of freedom in this process.

Appendix C: Asymptotic structure of equilibrium solutions

The present section scrutinizes equilibrium solutions determined from Eq. (B4) analytically in order to uncover further insight into their underlying structure. It is clear that equilibrium solutions consist of a nearly flat region near the wall for which $u \to -1$ (equivalently $\phi \to \pi$) and a spherical cap away from the wall and as $u \to 1$ (equivalently $\phi \to 0$). This observation allows us to approximate the solution within their respective regions.

Far from the wall, the interaction term $\Pi(h)$ in Eq. (B4) is generally small, particularly when ξ/R_0 is also small. When $\Pi(h)$ is absent, the solution to Eq. (B4) is exactly described

by a cap of a sphere of radius $R_c = cR_0$, for some constant c. Since in these cases we know that the pressure jump satisfies $\Delta p = 2\sigma/R_c$, we readily conclude from the definition of k in Appendix B that $c = 2/k$. From simple geometrical arguments concerning the droplet size, the way the coordinate system is defined (see Fig. 7) and the requirement that the droplet meets the substrate at the equilibrium angle $\theta_{\rm eq}$, we readily obtain that the droplet profile is essentially that of a circle of radius R_c which is shifted by a distance $R_c\cos^2(\theta_{\rm eq}/2)$ downwards along the z-axis with a contact line of radius:

$$r_c = R_c \sin\theta_{\rm eq}. \tag{C1}$$

Starting from the Cartesian representation of the circle

$$x^2 + y^2 + \left(z + R_c\cos^2\frac{\theta_{\rm eq}}{2}\right)^2 = R_c^2 \tag{C2}$$

and converting it to the spherical coordinate system, we find that the droplet surface is described by

$$r = R_c\left[-\cos^2\frac{\theta_{\rm eq}}{2}\cos\phi + \sqrt{1-\cos^4\frac{\theta_{\rm eq}}{2}\sin^2\phi}\right], \tag{C3}$$

noting that, as expected, the corresponding $g(u)$, namely

$$g(u) = c\left[-\cos^2\frac{\theta_{\rm eq}}{2}u + \sqrt{1-\cos^4\frac{\theta_{\rm eq}}{2}(1-u^2)}\right], \tag{C4}$$

satisfies Eq. (B4) with $k = 2/c$ when the $\Pi(h)$ term is not present. Based on these considerations, the half-height of the droplet, ℓ, is estimated as (see Fig. 7)

$$\ell = R_c\sin^2\frac{\theta_{\rm eq}}{2}, \tag{C5}$$

where corrections of order ξ/R_0 have been neglected.

Given that this model dictates smooth variations in curvature near the contact line with larger ξ/R_0 accommodating more gentle curvature variations, defining the contact angle cannot be done in a consistent manner. However, by invoking the spherical cap approximation, one can estimate the corresponding $\theta_{\rm eq}$ had ξ/R_0 been vanishingly small. This can be accomplished by utilizing the half-height of the droplet, which can be more accurately measured. Specifically, starting from the formula for the volume of a spherical cap in terms of $\tan(\theta_{\rm eq}/2)$ (see Appendix in [90]), we deduce that

$$\frac{8R_0^3}{r_c^3} = \tan\frac{\theta_{\rm eq}}{2}\left(3 + \tan^2\frac{\theta_{\rm eq}}{2}\right). \tag{C6}$$

Then, by combining Eq. (C1) with Eq. (C6), we obtain an expression for R_c in terms of R_0 and $\theta_{\rm eq}$, which, when substituted in Eq. (C5) yields

$$\tan^2\frac{\theta_{\rm eq}}{2} = \frac{3\ell^3}{R_0^3 - \ell^3}. \tag{C7}$$

Thus, the angle measured using Eq. (C7) may be used to compare with the value of $\theta_{\rm eq}$ imposed in Eq. (B4) as a means to assess the validity of the simplifying arguments invoked in Appendix A. Figure 8 shows a plot $\theta_{\rm eq}$ measured using Eq. (C7) as a function of the imposed angle $\pi/16 \le \theta_{\rm eq} \le 3\pi/4$, and for $\xi/R_0 = 0.1$ and 0.01. As expected, agreement improves as $\xi/R_0 \to 0$, but it remains generally better for obtuse angles compared to acute ones. The reason is that

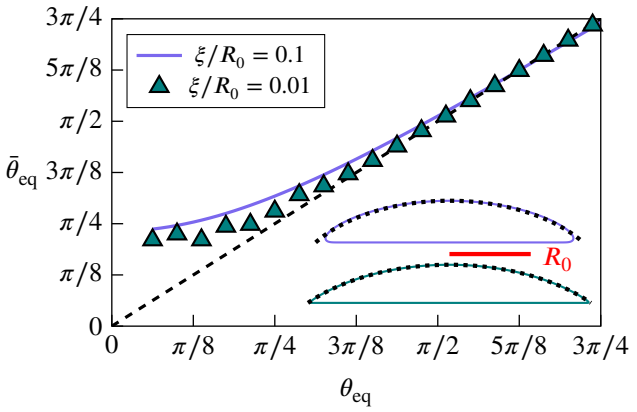

FIG. 8. Measured equilibrium contact angle, $\bar{\theta}_{\rm eq}$, using the height of the droplet and Eq. (C7), as a function of the imposed one, $\theta_{\rm eq}$, for $\xi/R_0 = 0.1$ (solid curve) and $\xi/R_0 = 0.01$ (symbols) compared with $\theta_{\rm eq} = \bar{\theta}_{\rm eq}$ (dashed line), which is expected to hold as $\xi/R_0 \to 0$. The inset shows droplet profiles for $\theta_{\rm eq} = \pi/4$ in the cases of $\xi/R_0 = 0.1$ (top; $\bar{\theta}_{\rm eq} \approx 0.32\pi$) and $\xi/R_0 = 0.01$ (bottom; $\bar{\theta}_{\rm eq} \approx 0.28\pi$). The red-colored line is a scale bar for R_0 which is used for scaling the profiles; the dotted curves correspond to fitted circular arcs matching the height and volume of the drop.

for smaller angles, the droplet's height decreases, making the assumption in Appendix A of an infinitely large wedge less relevant in this limit. Although the analysis in the Appendix could be revisited to account for finite-size effects, we chose not to pursue this approach, as the correction terms found did not significantly affect the results in the axisymmetric setting considered here.

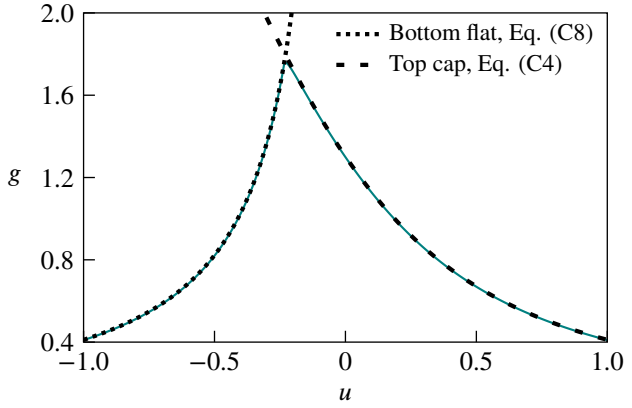

FIG. 9. Plot of g as a function of u when $\xi/R_0 = 0.01$ and $\theta_{\rm eq} = \pi/4$. Solid green line refers to the solution of Eq. (B4). Dotted and dashed curves correspond to the flattened and cap-shaped regions of the droplet given by Eqs. (C4) and (C8), respectively, using the measured angle $\theta_{\rm eq} \approx 0.28\pi$.

Also noteworthy is that Eq. (B4) admits planar solutions. The flattened part of the droplet, is assumed to lie on the plane $z = -\ell$ (see Fig. 7), which is expressed in spherical coordinates as $r = -R_c\sin^2(\theta_{\rm eq}/2)/\cos\phi$ [see Eq. (C5)]. Equivalently, using $r = R_0 g(u)$ with $u = \cos\phi$, we find that g is

approximated well as $u \to -1$ by

$$g(u) = -\frac{c \sin^2 \frac{\theta_{\rm eq}}{2}}{u}. \quad \text{(C8)}$$

Since planar solutions have no curvature ($\boldsymbol{\nabla}\cdot\hat{\boldsymbol{n}} = 0$), Eq. (B4) becomes

$$\left(\frac{\xi}{\delta}\right)^n - \left(\frac{\xi}{\delta}\right)^m = \frac{(n-m)\xi k}{R_0(m-1)(n-1)(1+\cos\theta_{\rm eq})} = \beta, \quad \text{(C9)}$$

noting that $\delta \neq \xi$ is the distance from the substrate, see Fig. 7). Solving this equation analytically is generally not possible. However we expect that $\delta < \xi$ and, in the limit of large drops ($\beta \to 0$), we have that $\delta \to \xi^-$. However, for certain combinations of n and m, an analytical solution may be found. For the combination of exponents used in the present study, $(n, m) = (6, 3)$, we find

$$\delta = \xi \left(\frac{2}{1+\sqrt{1+4\beta}}\right)^{1/3}. \quad \text{(C10)}$$

Figure 9 compares the solution to Eq. (B4) with the approximations given in Eqs. (C4) and (C8) for $\theta_{\rm eq} = \pi/4$ and $\xi/R_0 = 0.01$. An excellent agreement is observed when the angle used is not the one imposed in the model, but the one measured using Eq. (C7), found to be $\theta_{\rm eq} \approx 0.28\pi$.

[1] P.-G. De Gennes, Wetting: statics and dynamics, Reviews of Modern Physics **57**, 827 (1985).

[2] P.-G. Gennes, F. Brochard-Wyart, D. Quéré, *et al.*, *Capillarity and wetting phenomena: drops, bubbles, pearls, waves* (Springer, 2004).

[3] D. Bonn, J. Eggers, J. Indekeu, J. Meunier, and E. Rolley, Wetting and spreading, Reviews of Modern Physics **81**, 739 (2009).

[4] J. H. Snoeijer and B. Andreotti, Moving contact lines: scales, regimes, and dynamical transitions, Annual Review of Fluid Mechanics **45**, 269 (2013).

[5] B. Andreotti and J. H. Snoeijer, Statics and dynamics of soft wetting, Annual Review of Fluid Mechanics **52**, 285 (2020).

[6] M. J. De Ruijter, T. Blake, and J. De Coninck, Dynamic wetting studied by molecular modeling simulations of droplet spreading, Langmuir **15**, 7836 (1999).

[7] H. Kusumaatmaja, J. Leopoldes, A. Dupuis, and J. Yeomans, Drop dynamics on chemically patterned surfaces, Europhysics Letters **73**, 740 (2006).

[8] M. Sbragaglia, A. M. Peters, C. Pirat, B. M. Borkent, R. G. Lammertink, M. Wessling, and D. Lohse, Spontaneous breakdown of superhydrophobicity, Physical Review Letters **99**, 156001 (2007).

[9] H. Ding and P. D. Spelt, Inertial effects in droplet spreading: a comparison between diffuse-interface and level-set simulations, Journal of Fluid Mechanics **576**, 287 (2007).

[10] H. Kusumaatmaja, R. Vrancken, C. Bastiaansen, and J. Yeomans, Anisotropic drop morphologies on corrugated surfaces, Langmuir **24**, 7299 (2008).

[11] M. Blow, H. Kusumaatmaja, and J. Yeomans, Imbibition through an array of triangular posts, Journal of Physics: Condensed Matter **21**, 464125 (2009).

[12] N. Savva, S. Kalliadasis, and G. A. Pavliotis, Two-dimensional droplet spreading over random topographical substrates, Physical Review Letters **104**, 084501 (2010).

[13] N. Moradi, F. Varnik, and I. Steinbach, Roughness-gradient–induced spontaneous motion of droplets on hydrophobic surfaces: A lattice boltzmann study, Europhysics Letters **89**, 26006 (2010).

[14] M. Chinappi and C. M. Casciola, Intrinsic slip on hydrophobic self-assembled monolayer coatings, Physics of Fluids **22** (2010).

[15] D. Wheeler, J. A. Warren, and W. J. Boettinger, Modeling the early stages of reactive wetting, Physical Review E—Statistical, Nonlinear, and Soft Matter Physics **82**, 051601 (2010).

[16] N. Savva and S. Kalliadasis, Dynamics of moving contact lines: A comparison between slip and precursor film models, Europhysics Letters **94**, 64004 (2011).

[17] A. Carlson, M. Do-Quang, and G. Amberg, Dissipation in rapid dynamic wetting, Journal of Fluid Mechanics **682**, 213 (2011).

[18] A. Carlson, G. Bellani, and G. Amberg, Universality in dynamic wetting dominated by contact-line friction, Physical Review E—Statistical, Nonlinear, and Soft Matter Physics **85**, 045302 (2012).

[19] M. Gross and F. Varnik, Spreading dynamics of nanodrops: a lattice boltzmann study, International Journal of Modern Physics C **25**, 1340019 (2014).

[20] X. Frank, P. Perre, and H.-Z. Li, Lattice boltzmann investigation of droplet inertial spreading on various porous surfaces, Physical Review E **91**, 052405 (2015).

[21] D. Legendre and M. Maglio, Numerical simulation of spreading drops, Colloids and Surfaces A: Physicochemical and Engineering Aspects **432**, 29 (2013).

[22] D. Legendre and M. Maglio, Comparison between numerical models for the simulation of moving contact lines, Computers & Fluids **113**, 2 (2015).

[23] L. Baroudi and T. Lee, Effect of interfacial mass transport on inertial spreading of liquid droplets, Physics of Fluids **32** (2020).

[24] K. Guo, R. Chen, C. Wang, S. Qiu, W. Tian, and G. Su, Modeling of early stage droplet spreading based on numerical simulations, Nuclear Engineering and Design **369**, 110855 (2020).

[25] H. Chen, Q. Nie, and H. Fang, Dynamic behavior of droplets on confined porous substrates: A many-body dissipative particle dynamics study, Physics of Fluids **32** (2020).

[26] J. Du, N. T. Chamakos, A. G. Papathanasiou, and Q. Min, Initial spreading dynamics of a liquid droplet: The effects of wettability, liquid properties, and substrate topography, Physics of Fluids **33** (2021).

[27] R. Saiseau, C. Pedersen, A. Benjana, A. Carlson, U. Delabre, T. Salez, and J.-P. Delville, Near-critical spreading of droplets, Nature Communications **13**, 7442 (2022).

[28] F. Pelusi, F. Guglietta, M. Sega, O. Aouane, and J. Harting, A sharp interface approach for wetting dynamics of coated droplets and soft particles, Physics of Fluids **35**, 082126 (2023).

[29] Y. Liu, S. A. Hosseini, C. Liu, M. Feinberg, B. Dorschner, Z. Wang, and I. Karlin, Transition time of a bouncing drop, Physical Review Fluids **10**, 013602 (2025).

[30] A. Hosoi and L. Mahadevan, Peeling, healing, and bursting in a lubricated elastic sheet, Physical Review Letters **93**, 137802 (2004).

[31] J. R. Lister, G. G. Peng, and J. A. Neufeld, Viscous control of peeling an elastic sheet by bending and pulling, Physical Review Letters **111**, 154501 (2013).

[32] K. Doudrick, S. Liu, E. M. Mutunga, K. L. Klein, V. Damle, K. K. Varanasi, and K. Rykaczewski, Different shades of oxide: From nanoscale wetting mechanisms to contact printing of gallium-based liquid metals, Langmuir **30**, 6867 (2014).

[33] A. Carlson, Fluctuation assisted spreading of a fluid filled elastic blister, Journal of Fluid Mechanics **846**, 1076 (2018).

[34] E. Ni, T. Li, Y. Ruan, Y. Ma, Y. Wang, Y. Jiang, and H. Li, Modeling of wetting transition of liquid metals on organic liquid surfaces, Langmuir **37**, 9429 (2021).

[35] S. Poulain, A. Carlson, S. Mandre, and L. Mahadevan, Elastohydrodynamics of contact in adherent sheets, Journal of Fluid Mechanics **947**, A16 (2022).

[36] T. Sæter, C. Pedersen, J. H. Snoeijer, T. Salez, and A. Carlson, Coalescence of elastic blisters filled with a viscous fluid, Physical Review Letters **132**, 074001 (2024).

[37] S. Succi, *The lattice Boltzmann Equation* (Oxford University Press, 2018).

[38] T. Krüger, H. Kusumaatmaja, A. Kuzmin, O. Shardt, G. Silva, and E. M. Viggen, *The lattice Boltzmann method*, Vol. 10 (Springer, 2017) pp. 4–15.

[39] D. P. Silva, R. C. Coelho, I. Pagonabarraga, S. Succi, M. M. T. da Gama, and N. A. Araújo, Lattice boltzmann simulation of deformable fluid-filled bodies: progress and perspectives, Soft Matter (2024).

[40] F. Guglietta, M. Behr, L. Biferale, G. Falcucci, and M. Sbragaglia, On the effects of membrane viscosity on transient red blood cell dynamics, Soft Matter **16**, 6191 (2020).

[41] A. Rezghi and J. Zhang, Tank-treading dynamics of red blood cells in shear flow: On the membrane viscosity rheology, Biophysical Journal **121**, 3393 (2022).

[42] P. Li and J. Zhang, Similar but Distinct Roles of Membrane and Interior Fluid Viscosities in Capsule Dynamics in Shear Flows, Cardiovascular Engineering and Technology **12**, 232 (2021).

[43] F. Guglietta, M. Behr, L. Biferale, G. Falcucci, and M. Sbragaglia, Lattice Boltzmann simulations on the tumbling to tank-treading transition: effects of membrane viscosity, Philosophical Transactions of the Royal Society A: Mathematical, Physical and Engineering Sciences **379**, 20200395 (2021).

[44] F. Guglietta, M. Behr, G. Falcucci, and M. Sbragaglia, Loading and relaxation dynamics of a red blood cell, Soft Matter **17**, 5978 (2021).

[45] A. Rezghi, P. Li, and J. Zhang, Lateral migration of viscoelastic capsules in tube flow, Physics of Fluids **34** (2022).

[46] F. Guglietta, F. Pelusi, M. Sega, O. Aouane, and J. Harting, Suspensions of viscoelastic capsules: effect of membrane viscosity on transient dynamics, Journal of Fluid Mechanics **971**, A13 (2023).

[47] P. Li and J. Zhang, Finite-difference and integral schemes for maxwell viscous stress calculation in immersed boundary simulations of viscoelastic membranes, Biomechanics and Modeling in Mechanobiology **19**, 2667 (2020).

[48] F. Guglietta and F. Pelusi, Analytical prediction for the steady-state behavior of a confined drop with interface viscosity under shear flow, Physical Review Fluids **9**, 103603 (2024).

[49] P. Li and J. Zhang, A finite difference method with subsampling for immersed boundary simulations of the capsule dynamics with viscoelastic membranes, International Journal for Numerical Methods in Biomedical Engineering , e3200 (2019).

[50] D. Taglienti, F. Guglietta, and M. Sbragaglia, Reduced model for droplet dynamics in shear flows at finite capillary numbers, Physical Review Fluids **8**, 013603 (2023).

[51] D. Taglienti, F. Guglietta, and M. Sbragaglia, Droplet dynamics in homogeneous isotropic turbulence with the immersed boundary–lattice boltzmann method, Physical Review E **110** (2024).

[52] R. Benzi, S. Succi, and M. Vergassola, The lattice Boltzmann equation: theory and applications, Physics Reports **222**, 145 (1992).

[53] P. L. Bhatnagar, E. P. Gross, and M. Krook, A model for collision processes in gases. i. small amplitude processes in charged and neutral one-component systems, Physical Review **94**, 511 (1954).

[54] Z. Guo, C. Zheng, and B. Shi, Discrete lattice effects on the forcing term in the lattice Boltzmann method, Physical Review E **65**, 046308 (2002).

[55] J. Du, B. Fix, J. Glimm, X. Jia, X. Li, Y. Li, and L. Wu, A simple package for front tracking, Journal of Computational Physics **213**, 613 (2006).

[56] S. Shin and D. Juric, Modeling three-dimensional multiphase flow using a level contour reconstruction method for front tracking without connectivity, Journal of Computational Physics **180**, 427 (2002).

[57] A. Esmaeeli and G. Tryggvason, A front tracking method for computations of boiling in complex geometries, International Journal of Multiphase Flow **30**, 1037 (2004).

[58] G. Tryggvason, R. Scardovelli, and S. Zaleski, *Direct numerical simulations of gas–liquid multiphase flows* (Cambridge university press, 2011).

[59] A. Green and J. Adkins, *Large Elastic Deformations and Non-linear Continuum Mechanics* (Clarendon Press, 1960).

[60] D. Barthès-Biesel and J. Rallison, The time-dependent deformation of a capsule freely suspended in a linear shear flow, Journal of Fluid Mechanics **113**, 251 (1981).

[61] Y. I. Dimitrienko, *Nonlinear continuum mechanics and large inelastic deformations*, Vol. 174 (Springer Science & Business Media, 2010).

[62] T. Krüger, *Computer Simulation Study of Collective Phenomena in Dense Suspensions of Red Blood Cells under Shear* (Vieweg+Teubner Verlag, 2012).

[63] J. Göhl, A. Mark, S. Sasic, and F. Edelvik, An immersed boundary based dynamic contact angle framework for handling complex surfaces of mixed wettabilities, International Journal of Multiphase Flow **109**, 164 (2018).

[64] N. T. Chamakos, M. E. Kavousanakis, and A. G. Papathanasiou, Enabling efficient energy barrier computations of wetting transitions on geometrically patterned surfaces, Soft Matter **9**, 9624 (2013).

[65] G. Karapetsas, N. T. Chamakos, and A. G. Papathanasiou, Efficient modelling of droplet dynamics on com-

plex surfaces, Journal of Physics: Condensed Matter **28**, 085101 (2016).
[66] J. N. Israelachvili, *Intermolecular and surface forces* (Academic press, 2011).
[67] F. Brochard-Wyart, J. M. Di Meglio, D. Quére, and P. G. De Gennes, Spreading of nonvolatile liquids in a continuum picture, Langmuir **7**, 335 (1991).
[68] J. Eggers, Contact line motion for partially wetting fluids, Physical Review E—Statistical, Nonlinear, and Soft Matter Physics **72**, 061605 (2005).
[69] N. T. Chamakos, M. E. Kavousanakis, A. G. Boudouvis, and A. G. Papathanasiou, Droplet spreading on rough surfaces: Tackling the contact line boundary condition, Physics of Fluids **28** (2016).
[70] M. Wilczek, W. Tewes, S. Engelnkemper, S. V. Gurevich, and U. Thiele, Sliding drops: Ensemble statistics from single drop bifurcations, Physical Review Letters **119**, 204501 (2017).
[71] S. Zitz, A. Scagliarini, S. Maddu, A. A. Darhuber, and J. Harting, Lattice Boltzmann method for thin-liquid-film hydrodynamics, Physical Review E **100**, 033313 (2019).
[72] A.-L. Biance, C. Clanet, and D. Quéré, First steps in the spreading of a liquid droplet, Physical Review E **69**, 016301 (2004).
[73] J. C. Bird, S. Mandre, and H. A. Stone, Short-time dynamics of partial wetting, Physical Review Letters **100**, 234501 (2008).
[74] L. Courbin, J. C. Bird, M. Reyssat, and H. A. Stone, Dynamics of wetting: from inertial spreading to viscous imbibition, Journal of Physics: Condensed Matter **21**, 464127 (2009).
[75] K. G. Winkels, J. H. Weijs, A. Eddi, and J. H. Snoeijer, Initial spreading of low-viscosity drops on partially wetting surfaces, Physical Review E **85**, 055301 (2012).
[76] A. Eddi, K. G. Winkels, and J. H. Snoeijer, Short time dynamics of viscous drop spreading, Physics of Fluids **25** (2013).
[77] L. Chen and E. Bonaccurso, Effects of surface wettability and liquid viscosity on the dynamic wetting of individual drops, Physical Review E **90**, 022401 (2014).
[78] B. M. Jose and T. Cubaud, Role of viscosity coefficients during spreading and coalescence of droplets in liquids, Physical Review Fluids **2**, 111601 (2017).
[79] F. Pelusi, M. Sega, and J. Harting, Liquid film rupture beyond the thin-film equation: A multi-component lattice Boltzmann study, Physics of Fluids **34**, 062109 (2022).
[80] D. G. Aarts, H. N. Lekkerkerker, H. Guo, G. H. Wegdam, and D. Bonn, Hydrodynamics of droplet coalescence, Physical Review Letters **95**, 164503 (2005).
[81] J. Eggers, J. R. Lister, and H. A. Stone, Coalescence of liquid drops, Journal of Fluid Mechanics **401**, 293 (1999).
[82] L. Duchemin, J. Eggers, and C. Josserand, Inviscid coalescence of drops, Journal of Fluid Mechanics **487**, 167 (2003).
[83] M. Wu, T. Cubaud, and C.-M. Ho, Scaling law in liquid drop coalescence driven by surface tension, Physics of Fluids **16**, L51 (2004).
[84] S. Thoroddsen, K. Takehara, and T. Etoh, The coalescence speed of a pendent and a sessile drop, Journal of Fluid Mechanics **527**, 85 (2005).
[85] S. C. Case and S. R. Nagel, Coalescence in low-viscosity liquids, Physical Review Letters **100**, 084503 (2008).
[86] J. D. Paulsen, J. C. Burton, and S. R. Nagel, Viscous to inertial crossover in liquid drop coalescence, Physical Review Letters **106**, 114501 (2011).
[87] L. Tanner, The spreading of silicone oil drops on horizontal surfaces, Journal of Physics D: Applied Physics **12**, 1473 (1979).
[88] O. V. Voinov, Hydrodynamics of wetting, Fluid Dynamics **11**, 714 (1976).
[89] N. Chamakos, *Design of micro-and nano-structured surfaces with tunable wettability*, Ph.D. thesis (2017).
[90] A. D. Demou and N. Savva, Hybrid ai-analytical modeling of droplet dynamics on inclined heterogeneous surfaces, Mathematics **12**, 1188 (2024).
[91] A. D. Demou and N. Savva, Ai-assisted modeling of capillary-driven droplet dynamics, Data-Centric Engineering **4**, e24 (2023).
[92] A. Pressley, *Elementary Differential Geometry* (Springer London, 2010).
[93] E. A. Boucher, Capillary phenomena: Properties of systems with fluid/fluid interfaces, Reports on Progress in Physics **43**, 497 (1980).
[94] E. Bellantoni, F. Guglietta, F. Pelusi, M. Desbrun, K. Um, M. Nicolaou, N. Savva, and M. Sbragaglia, Public dataset: 10.5281/zenodo.15096775 (2025).